So-Called Lamina Cribrosa Defects May Mitigate IOP-Induced Neural Tissue Insult

Andrew P. Voorhees,[1] Yi Hua,[1] Bryn L. Brazile,[1] Bingrui Wang,[1,2] Susannah Waxman,[1] Joel S. Schuman,[3–6] and Ian A. Sigal[1,7–9]

[1]Department of Ophthalmology, University of Pittsburgh, Pittsburgh, Pennsylvania, United States
[2]School of Mechanical Engineering, Southwest Jiaotong University, Chengdu, Sichuan, China
[3]Department of Ophthalmology, NYU Langone Health, New York University Grossman School of Medicine, New York, New York, United States
[4]Center for Neural Science, New York University, New York, New York, United States
[5]Department of Biomedical Engineering, New York University Tandon School of Engineering, Brooklyn, New York, United States
[6]Department of Physiology and Neuroscience, Neuroscience Institute, NYU Langone Health, New York University Grossman School of Medicine, New York, New York, United States
[7]Department of Bioengineering, University of Pittsburgh, Pittsburgh, Pennsylvania, United States
[8]McGowan Institute for Regenerative Medicine, University of Pittsburgh Medical Center and University of Pittsburgh, Pittsburgh, Pennsylvania, United States
[9]Louis J. Fox Center for Vision Restoration, University of Pittsburgh Medical Center and University of Pittsburgh, Pittsburgh, Pennsylvania, United States

Correspondence: Ian A. Sigal, Laboratory of Ocular Biomechanics, Department of Ophthalmology, Eye and Ear Institute, University of Pittsburgh School of Medicine, 203 Lothrop Street, Room 930, Pittsburgh, PA 15213, USA; ian@OcularBiomechanics.com.

APV and YH contributed equally to the work presented here and should therefore be regarded as equivalent authors.

Received: July 25, 2020
Accepted: October 20, 2020
Published: November 9, 2020

Citation: Voorhees AP, Hua Y, Brazile BL, et al. So-called lamina cribrosa defects may mitigate IOP-induced neural tissue insult. *Invest Ophthalmol Vis Sci.* 2020;61(13):15. https://doi.org/10.1167/iovs.61.13.15

Purpose. The prevailing theory about the function of lamina cribrosa (LC) connective tissues is that they provide structural support to adjacent neural tissues. Missing connective tissues would compromise this support and therefore are regarded as "LC defects", despite scarce actual evidence of their role. We examined how so-called LC defects alter IOP-related mechanical insult to the LC neural tissues.

Methods. We built numerical models incorporating LC microstructure from polarized light microscopy images. To simulate LC defects of varying sizes, individual beams were progressively removed. We then compared intraocular pressure (IOP)-induced neural tissue deformations between models with and without defects. To better understand the consequences of defect development, we also compared neural tissue deformations between models with partial and complete loss of a beam.

Results. The maximum stretch of neural tissues decreased non-monotonically with defect size. Maximum stretch in the model with the largest defect decreased by 40% in comparison to the model with no defects. Partial loss of a beam increased the maximum stretch of neural tissues in its adjacent pores by 162%, compared with 63% in the model with complete loss of a beam.

Conclusions. Missing LC connective tissues can mitigate IOP-induced neural tissue insult, suggesting that the role of the LC connective tissues is more complex than simply fortifying against IOP. The numerical models further predict that partial loss of a beam is biomechanically considerably worse than complete loss of a beam, perhaps explaining why defects have been reported clinically but partial beams have not.

Keywords: biomechanics, modeling, lamina cribrosa, optic nerve head, defect, collagen

Studies of the lamina cribrosa (LC) architecture in vivo using optical coherence tomography[1–3] or ex vivo using histology[4,5] describe regions of missing LC connective tissues, discernible as holes, pits, disinsertions, gaps, or localized irregularities in the LC. A prevailing theory about the function of LC connective tissues is that they provide structural support to the adjacent neural tissues, including LC astrocytes and unmyelinated retinal ganglion cell axons.[6–12] A focal decrease or absence of connective tissues would compromise this support, aggravating intraocular pressure (IOP)-induced mechanical insult to neural tissues.[5,13–15] This, in turn, would potentially increase the risk of neural tissue damage and vision loss, explaining why these foci of missing connective tissues are regarded as "LC defects."[16–20] Several studies have searched for an association between so-called LC defects and neural tissue damage, but the evidence for this is not conclusive.[16–20] Furthermore, the actual biomechanical impact of LC defects on the adjacent neural tissues remains undetermined. We have recently developed biomechanical models that

explicitly take into account the microstructure of the LC.[21,22] These models suggest that IOP-induced mechanical insult to neural tissues is highly sensitive to the local LC beam architecture, perhaps as much as or more than it is sensitive to the overall connective tissue density.[23–27]

Our goal was to examine how LC defects alter IOP-related mechanical insult to neural tissues within the LC. To accomplish this goal, we modified our microstructure-based models[21,22] to represent LC defects of varying sizes. We then compared IOP-induced neural tissue deformations between models with and without LC defects.

Methods

This study is based on numerical models reported previously.[21,22] Modeling methodology, assumptions, and a discussion of the strengths and limitations of the models can be found therein. Briefly, our models were constructed from data obtained from histological sections of the sheep optic nerve head (ONH) imaged using polarized light microscopy.[28–36] We first modeled the ONH at a mesoscale level. The mesoscale model was then used to provide boundary conditions for a high-resolution microscale model of the LC region that explicitly incorporates distinct collagen beams and neural tissues. To simulate LC defects, individual beams were progressively removed from the microscale model. We then examined how these changes altered IOP-induced mechanical insult to neural tissues of the LC. Finally, we modified the microscale model to produce two models with partial and complete loss of a beam. These models were intended to help understand the effects of an ostensibly minor LC defect. The steps outlined above are described in detail below.

Mesoscale Modeling

Our modeling approach is outlined in Figure 1. Six serial histological sections (30-µm section thickness) through the ONH were obtained from a normal sheep eye fixed at an IOP of 5 mm Hg. These sections were chosen because they included the full lamina portion of the ONH and were free of histological artifacts, such as broken or missing tissue or section folds. These sections were then imaged with polarized light microscopy at a resolution of 4.4 µm/pixel and registered to one another to form a volumetric image stack. The thickness-averaged pixel energy, a measure of collagen density, and the thickness-averaged pixel orientation for the set of images were calculated for use as the basis for the mesoscale model.[21,22]

For the mesoscale model, we followed an approach similar to the one by Zhang et al.[24]; however, the ONH was modeled as a circular disk with a thickness equal to 5% of the diameter, rather than as a square. Quadratic tetrahedral elements with an average edge length of 112 µm were used for the mesh.

The ONH tissue was modeled as a fiber-reinforced composite, with fibers modeled using an exponential power law and the ground substance modeled as a neo-Hookean solid.[37] The strain energy density for the collagenous tissue was weighted by the density of collagen fibers, which we determined using polarized light microscopy.[36] The weighting was chosen such that any element with an average pixel energy value equal to the average pixel energy value of all elements belonging to the sclera would have the mechanical properties matching those of human scleral collagen (Table).[38] A von Mises distribution was used to model the angular distribution of collagen fibers; however, we did not use direct measurements of the collagen fiber angular distribution by polarized light microscopy. Instead, we chose a fiber dispersion factor of 0.6, as this was found to be a reasonable estimate in the mesoscale study from which we obtained mechanical properties for scleral collagen.[38]

To simulate the effects of IOP, a uniform outward boundary pressure was applied to the edges of the disk (diameter, 11.5 mm) to mimic the effects of hoop stresses. We applied the boundary pressure farther away from the LC to better model the mechanics of the scleral tissue. Based on the law of Laplace,[39] we determined that the hoop stress multiplier for the sheep eye was 10× IOP. Thus, to model an IOP increase of 20 mm Hg, a boundary pressure of 200 mm Hg was applied (26.7 kPa). An extensive discussion of the rationale and implications of these choices has been presented previously.[21,22,24]

Microscale Modeling

Baseline Microscale Model Without a Defect. The microscale model was constructed from histological section images acquired at a resolution of 0.73 µm/pixel.[28,29,32] The images were registered to the ones that were used to construct the mesoscale model. Collagen density was used as the basis for the two-dimensional (2D) image segmentation. For microscale modeling, we selected a region in the LC periphery where defects are located most often (Fig. 1).[14,18,40] We provide further details about our choice later in the Discussion section. The selected region had clearly defined collagen beams and no evidence of defects. An intensity-based threshold was used to segment the collagen beams and neural tissues within lamina pores. Segmentations were verified by someone familiar with LC microstructure.

From the segmented images, LC beams and neural tissues were reconstructed in three dimensions (3D) based on the assumption that beams had a circular cross-section. Our circular beam reconstruction method produced a model that was symmetric about the coronal plane; thus, the deformation was also assumed to be symmetric about this plane. This allowed us to model only half of the reconstructed LC volume. The LC beams and neural tissues were modeled using a quadratic tetrahedral mesh with an average edge length of 8 µm.

Mechanical properties of the LC beams were the same as those of the sclera used in the mesoscale model.[38] The mean fiber orientation for each LC beam element was determined from the polarized light microscopy fiber orientation data. A von Mises distribution with a fiber dispersion factor of 2 was used to model the angular distribution of collagen fibers in the LC beams. The mechanical properties of neural tissues were based on data from guinea pig white matter (Table).[41] Neural tissues were modeled as compressible to account for the potential motion of the fluid into and out of neural tissues of the LC. Future studies may benefit from distinguishing whether the axons in the region simulated are myelinated or unmyelinated, as this might affect their mechanical properties.[42] A thorough discussion of the tissue mechanical properties used in this model and their influence on model predictions can be found in our recent report.[22]

Displacement-driven boundary conditions were obtained by linearly interpolating the displacement predicted from

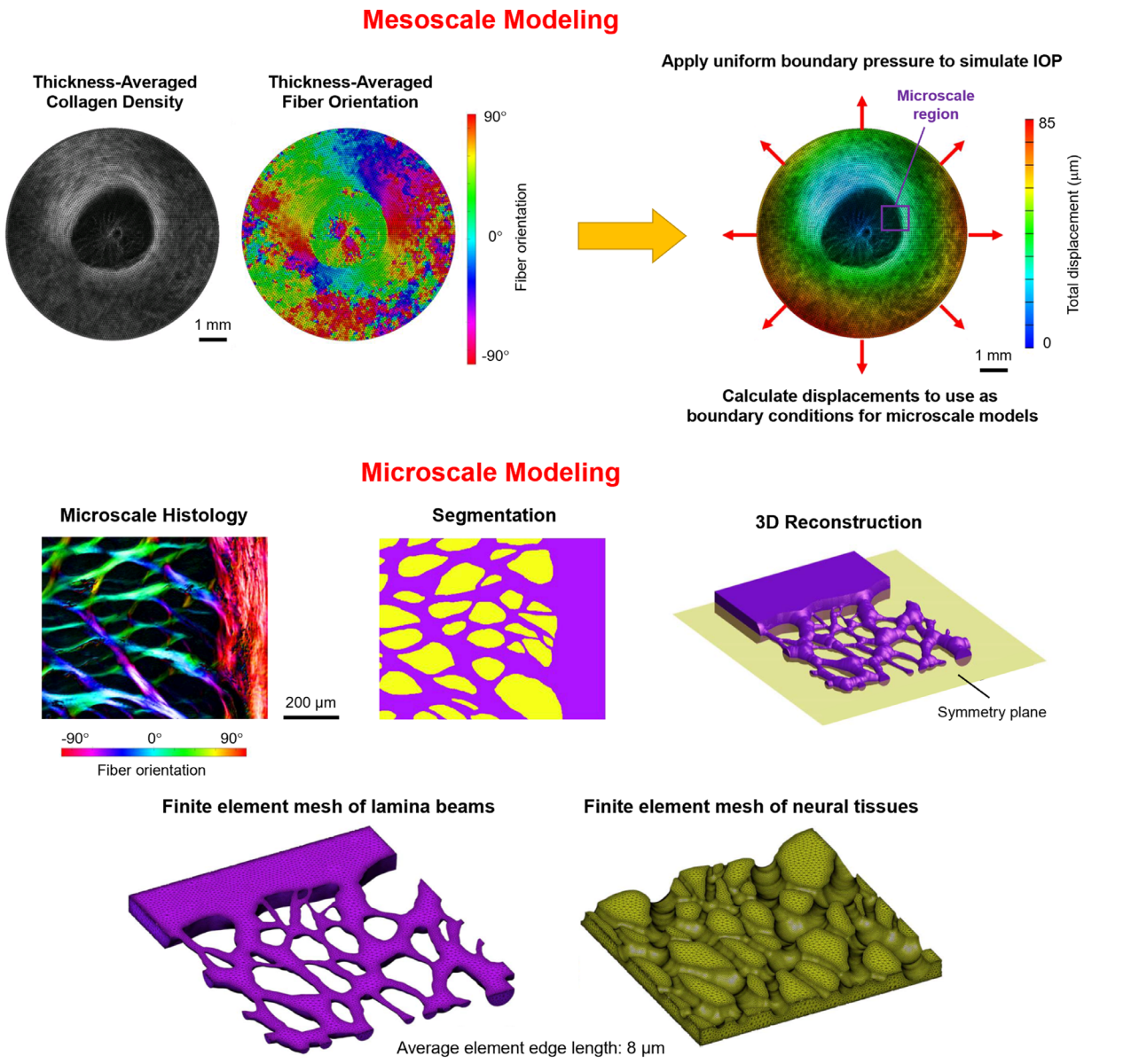

Figure 1. Multiscale modeling approach modified from References 21 and 22. For the mesoscale model (*top*), tissue mechanical properties were based on fiber density and orientation information from serial histology. Uniform boundary pressure was applied to simulate the hoop stress caused by IOP. Displacement predictions were obtained from the mesoscale model to use as boundary conditions for the microscale model (*bottom*). For the microscale model, the lamina cribrosa region of histological sections was imaged at high resolution and segmented into the laminar beams and neural tissues. A 3D reconstruction of the beams was used as the basis for the finite element mesh. Fiber orientation was taken directly from polarized light microscopy images.

Table. Tissue Mechanical Properties

Parameter	Connective Tissues	Neural Tissues
ξ, fiber stiffness (kPa)	1600	69.4
α, fiber nonlinearity	120	1
C_1, first Mooney–Rivlin constant (kPa)	150	0.876
C_2, second Mooney–Rivlin constant (kPa)	0	0.614
κ, fiber dispersion	2	2
K, bulk modulus (kPa)	5000	0.412

Investigative Ophthalmology & Visual Science

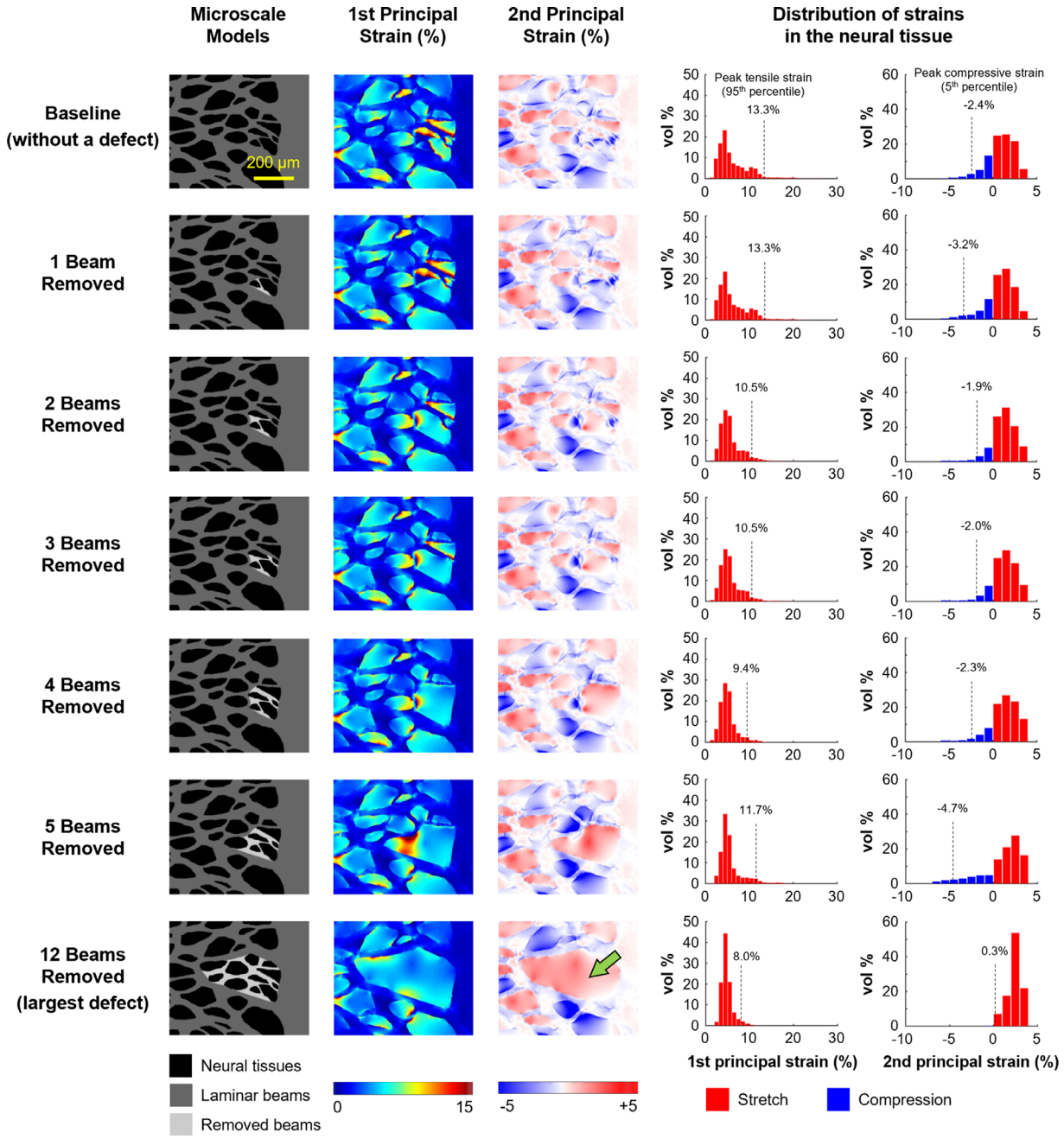

Figure 2. Contour plots of the predicted first (*second column*) and second (*third column*) principal strains by the microscale models with and without defects (*first column*). Removed beams are shown in a different *gray* to aid recognizing the changes. The distributions of the first and second principal strains in pores forming the defect are shown in the *fourth* and *fifth columns*, respectively. The *vertical dotted line* shows the maximum (95th percentile) first principal strain and minimum (5th percentile) second principal strain, corresponding to the maximum stretch and compression, respectively. In the baseline model without a defect (*first row*), there was a wide variation in the first principal strain from one pore to another. The maximum first principal strain in models with defects decreased, but not monotonically, with the size of the defect. Interestingly, in the model with the largest defect (*bottom row*), the second principal strain in the defect itself was positive (*green arrow*), suggesting no neural tissue compression in the defect region. vol, volume fraction.

the mesoscale model to the location of nodes on the boundary of the microscale model mesh.

Microscale Models With LC Defects. We modified the baseline model to construct microscale models with LC defects of varying sizes. Specifically, we progressively removed individual beams from the baseline model (Figs. 2, 3). We defined an LC beam as an unbranched tract or segment between beam junctions or branching points. The number of beams removed was 1, 2, 3, 4, 5, and 12 (largest defect). As the size of the defect was small compared with the lamina, we assumed that the LC defect would not influence the displacement predicted by the mesoscale model. Therefore, we assigned the same displacement-driven boundary condition for models with LC defects as that for the baseline model. The mechanical properties of tissues in models with LC defects were also

Investigative Ophthalmology & Visual Science

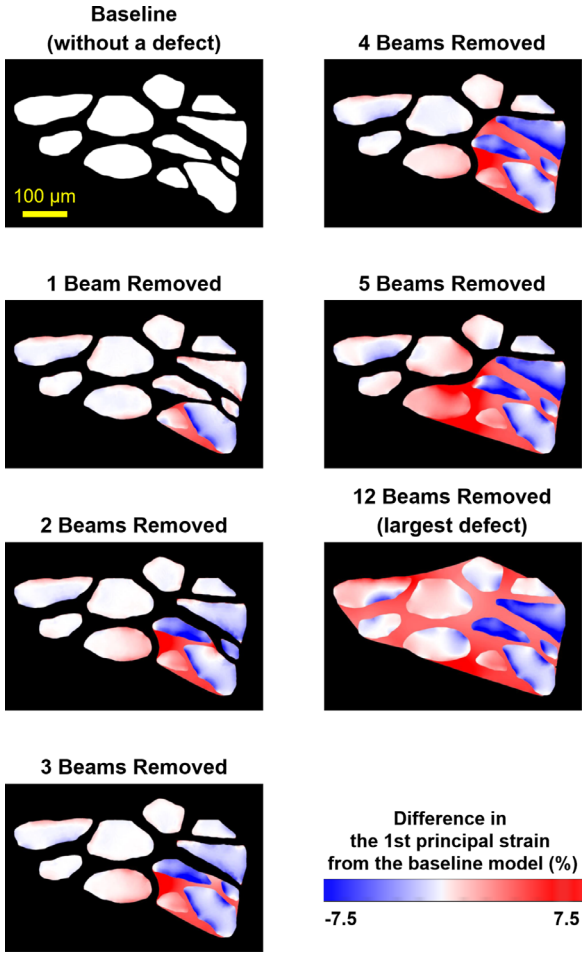

Figure 3. Contour plots of the difference in the first principal strain between the baseline model (without a defect) and models with defects. For clarity, only a partial region of the microscale model is shown. *White* color indicates that there was no change in the strain. *Red* and *blue* colors indicate that enlarging the defect by removing laminar beams increased or decreased the strain, respectively. Removing a beam caused an increase in strain in the exact location where the beam used to be. This is not surprising, as the beam was replaced by the softer neural tissues. For a fair comparison, we did not consider the strain changes in these regions for the strain quantifications.

assumed the same as those in the baseline model. The beams removed were replaced with neural tissues; thus, the models represent LCs with different architectures, not remodeling or defect progression. The rationale and interpretation are addressed in more detail in the Discussion section. To better understand the effects of LC beam loss, we also constructed two microscale models with partial and complete loss of a beam (Fig. 4). We chose to model partial loss of a beam over beam thinning because it can provide an upper-bound estimation of the influence of beam thinning on IOP-induced mechanical insult to neural tissues. To model partial loss of a beam, a beam was cut transversely in a small area.

Mechanical Analysis

We present results only from the microscale models. Strains reported herein are for elements along the symmetry surface of the model for which the geometry corresponded directly to the histological image. The first and second principal strains were calculated from the in-plane strain components. The first principal strain represents the largest strain, and the second principal strain represents the strain in the direction orthogonal to the direction of the first principal strain. Positive strains represent stretch, whereas negative ones represent compression. When both strains are positive, the tissue is in biaxial tension. When both strains are negative, the tissue is in biaxial compression. As a measure of the peak strain, we used the 95th percentile strain computed using volume weighting to compensate for different sized elements and to account for potential numerical artifacts in corners.[43]

Statistical Analysis

Using linear mixed-effects models, we determined whether IOP-induced neural tissue strains were significantly different between models with and without LC defects. Linear mixed-effects models are linear models that incorporate fixed and random variables. Fixed variables are the variables of interest, which in this case are the strain measurements. Random variables are factors that may affect the sampling population, such as the number of measurements in different models. We removed the spatial autocorrelation by specifying a rational quadratic spatial correlation structure using the Cartesian distance between the elements in each model.[44] We used $\alpha = 0.01$ to establish significance. Statistical analysis was done with R 3.5.1 (R Foundation for Statistical Computing, Vienna, Austria).

Software

FEBio 2.3.0 was used for all finite element analysis.[45] PaintShop Pro X2 (Corel Corp., Ottawa, ON, Canada) was used for 2D manual segmentation of microscale models. Fiji Is Just ImageJ (FIJI) (http://imagej.nih.gov/ij/; provided in the public domain by the National Institutes of Health, Bethesda, MD, USA) was used for 2D image skeletonization and analysis of polarized light microscopy images including image stitching.[28,29,32] Custom code and the GIBBON toolbox[46] for MATLAB 2015b (MathWorks, Natick, MA, USA) were used to create the mesoscale meshes, generate segmented volumes, register microscale models to mesoscale models, write FEBio input files, and analyze data. Avizo Wind 8.0.1 (Thermo Fisher Scientific, Hillsboro, OR, USA) was used to register histological sections and create the meshes used to make the microscale models.

Results

Figure 2 shows the first and second principal strains predicted by the microscale models with and without defects. In the baseline model without a defect, there was a wide variation in the first principal strain from one pore to another, with median (50th percentile) and maximum (95th percentile) strains of 5.1% and 13.3%, respectively. The lowest strains were reached in the model with the largest defect, with median and maximum strains 11.3% and 40.0% lower than those in the baseline model, respectively. The second principal strain in the baseline model was positive in the majority of pores, indicating a state of the biaxial stretch, but it was negative in several pores, indicating tissue compression in the direction of the second principal strain.

Investigative Ophthalmology & Visual Science

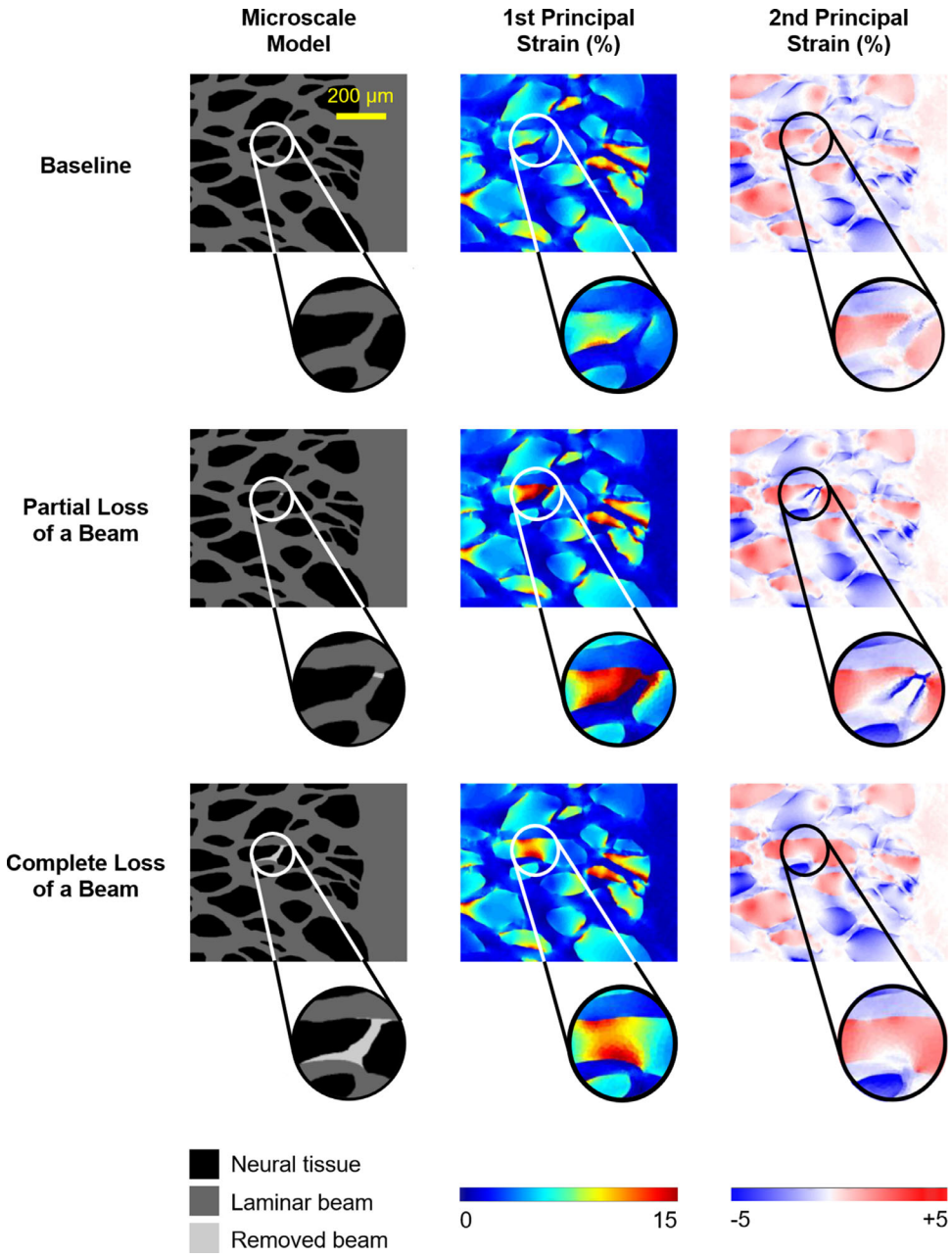

Figure 4. The first (*middle column*) and second (*right column*) principal strains predicted by the microscale models without a defect (baseline model, *first row*), with partial loss of a beam (*second row*), and with complete loss of a beam (*third row*). Surprisingly, partial loss of a beam induced much larger first and second principal strains in neural tissues than complete loss of a beam.

Interestingly, in the model with the largest defect, the second principal strain in the defect region was positive, suggesting no neural tissue compression.

For ease of visualizing the impact of LC defects on IOP-induced stretch to neural tissues, we calculated the difference in the first principal strain between the baseline model and models with LC defects. The results are shown in Figure 3. It is not surprising that removing a beam caused an increase in strain in the exact location where the beam used to be, as the beam was replaced by the softer neural tissues. For a fair comparison, we did not consider the strain changes in these regions for the strain quantifications.

Figure 4 shows the first and second principal strains predicted by the microscale models with partial and complete loss of a beam. Corresponding box plots are shown in Figure 5. We found that partial loss of a beam induced much larger first and second principal strains in neural tissues than complete loss of a beam.

Discussion

The role of LC defects in neural tissue biomechanics remains unclear. Our goal was to examine how LC defects alter IOP-related mechanical insult to neural tissues within the LC. We

Investigative Ophthalmology & Visual Science

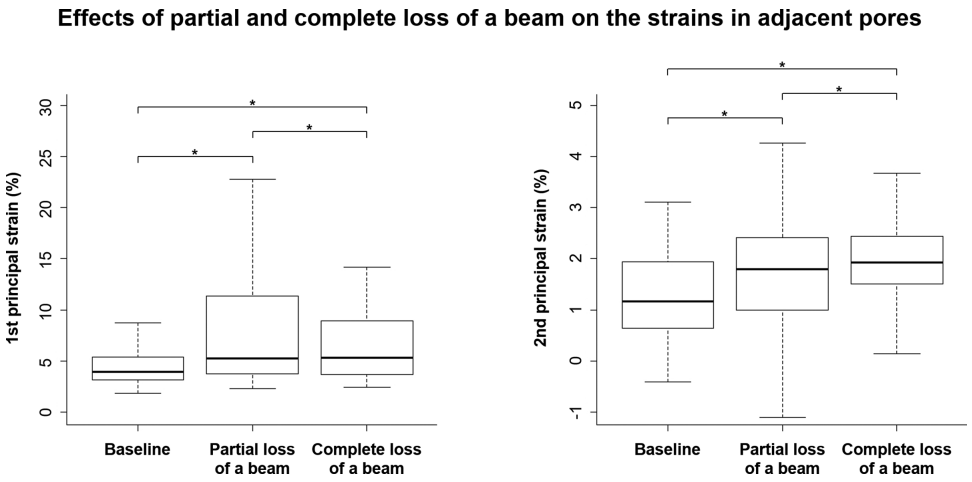

Figure 5. Effects of partial and complete loss of a beam on the strains in the adjacent pores. (*Left*) Boxplots of the first principal strain. (*Right*) Boxplots of the second principal strain. Partial loss of a beam induced higher strains in adjacent pores than complete loss of a beam. For example, partial loss of a beam increased the maximum first principal strain in adjacent pores by 162% compared to the baseline model, whereas the strain was increased by only 63% when the beam was completely lost. $^{*}P < 0.001$.

found that missing LC connective tissues can mitigate IOP-induced neural tissue insult. Specifically, we highlight two main findings: (1) missing beams can lower IOP-induced mechanical insult to the surrounding neural tissues, and (2) partial loss of a beam is biomechanically much worse than complete loss of a beam. These results suggest that the role of the LC connective tissues is more complex than simply fortifying against IOP. Below we discuss each of these findings in detail.

Our models predict that missing beams can lower IOP-induced mechanical insult to the surrounding neural tissues. This is different from the traditional assumption that loss of beams would necessarily weaken the trabecular structure of the LC and thus increase insult to neural tissues.[5] We propose two ways to understand this finding. The first one is illustrated in Figure 6. Because the beams are stiffer than the neural tissues, a beam can cause concentrations of strain when the loading is not aligned to the beam. If the beam is removed, the strain concentrations in the neural tissue are relieved. Second, in a previous study, we have shown that the peak tensile strains in the neural tissues of LC pores were negatively correlated with the degree of pore convexity (a shape that curves or bulges outward).[21] Therefore, if the shape of the pore formed by loss of beams is more convex than the original one, the peak tensile strains in neural tissues within that pore would decrease.

We admit that it was initially a surprise to us to observe that partial loss of a beam is biomechanically much worse than complete loss of a beam. We had anticipated that, because the partial loss of a beam represents a minor loss of stiff connective tissues, it would result in a more modest effect. The underlying mechanisms can be understood as follows (Fig. 6): A beam only has to become broken to lose much of its ability to carry load; therefore, IOP-induced stretch along the beam ends up concentrated in the soft tissues that have replaced the broken beam. This region is much smaller in a partially lost beam than in the case of complete beam loss. For the same level of stretch, the stretch-induced tensile strain in a smaller region would be larger.

It is interesting to consider our findings in the context of studies that have shown that mechanical strain protects collagen fibrils from enzymatic digestion and that unstrained fibrils are preferentially degraded.[47–49] Strain stabilization is easily seen as an important mechanism in the development of fiber networks with preferred orientation; however, the ability of proteases to rapidly degrade unstrained collagen fibrils may have an important protective role in limiting high strain concentrations, which could lead to further mechanical insult. This may also help explain clinical observations of LC defects in the form of complete loss of collagen beams.[50,51]

Because of the shared trabecular architecture, the LC has been compared with trabecular bone.[5,12,52,53] However, our results suggest that there are important differences. In trabecular bone, the mechanical disadvantages increase monotonically with the amount of load-bearing bone lost.[54,55] We have shown that this is not the case with LC beams. The key to understanding the difference with the LC is that, when analyzing thinning of bone trabeculae, the focus is typically on understanding the effects on the strength and load-bearing capacity of the trabeculae themselves. Any bone loss would weaken the structure. Depending on the location it could weaken it by much or by a little. For the LC, our interest in this work has been the effect of removing LC trabeculae on the adjacent neural tissues, which is not straightforward. Loss of an LC beam may weaken the LC structure slightly, but it is possible that the most important effect could be an improvement in the insult to the adjacent neural tissues.

We would like to caution that our results should not be interpreted as suggesting that the LC does not provide any structural support to the neural tissues or, worse, that removing all beams would provide the most biomechanical benefit to the neural tissues. Our interpretation is that the results suggest that we should be careful when interpreting the role of the LC at different scales. Studies from us[8,22,23,27,56–59] and others[24,53,60–62] consistently point to the important biomechanical advantages that a macro- and mesoscale collagenous LC region provides to the neural tissues within the ONH. Our results suggest that this is not necessarily as clear an answer in the pore and beam microscale. Because many key aspects of the mechanobiology[38,63–65] of

Investigative Ophthalmology & Visual Science

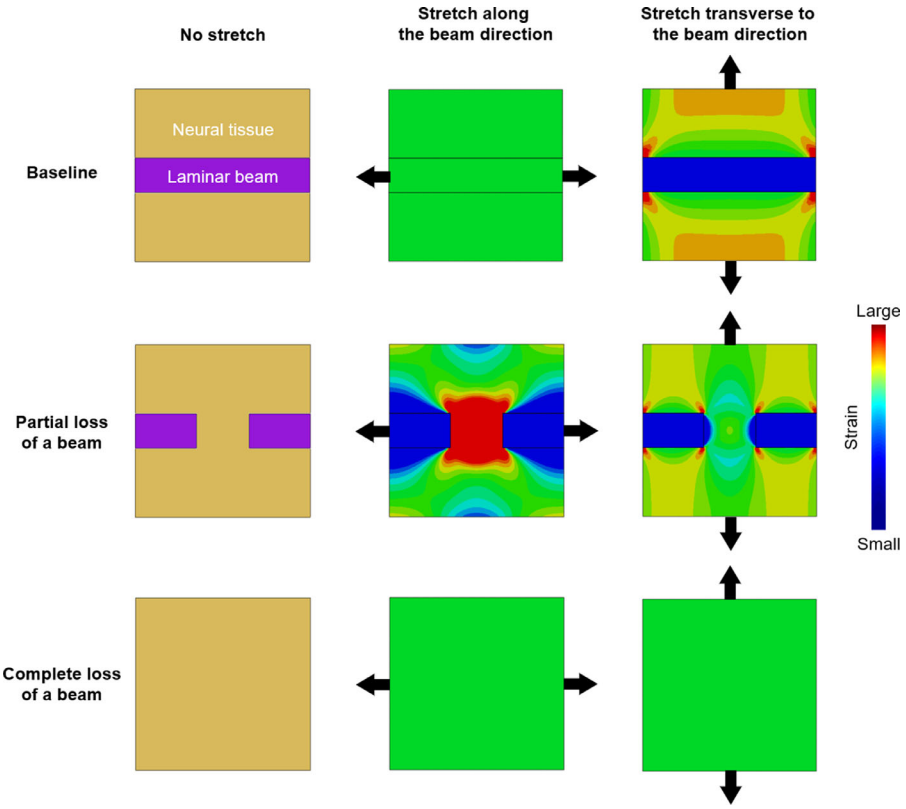

Figure 6. A schematic to explain the mechanisms underlying the two potentially non-intuitive findings of this work: (1) missing beams can lower IOP-induced mechanical insult to the surrounding neural tissues, and (2) partial loss of a beam is biomechanically much worse than complete loss of a beam. We show three cases (*left column*) to represent neural tissues adjacent to an intact beam (baseline), a partial beam (partial loss), and no beam (complete loss). We then examine the stretch-induced tensile strains in the neural tissues caused by stretching the region in the longitudinal (*middle column*) or transverse (*right column*) directions relative to the beam. To simplify comparisons, strains are shown in the undeformed geometry. In the baseline case (*top row*), when the stretch is transverse to the beam direction (*top right*), there are strain concentrations in the neural tissues near the beam. When the stretch is along the beam (*top center*), the strain is uniform. In most of the neural tissues this uniform strain is lower than the strain in the transverse loading. Because the beam is stiffer than the neural tissues, in the case with transverse loading, large deformations were avoided. These deformations were, instead, suffered by the neural tissues. In the case of complete loss of a beam (*bottom row*), the neural tissue strain is uniform regardless of the stretch direction. Compared to the baseline case, the magnitude of strain is the same when the stretch is along the beam direction and smaller when the stretch is transverse to the beam direction. Thus, a missing beam lowers the deformation for loading components that are not longitudinal to the beam. In the case of partial loss of a beam (*middle row*), when the stretch is along the beam direction (*middle row*, *center column*), the beam acts as a "tweezer" to stretch the neural tissues between the ends of the "broken" beam, causing large strain concentrations in this region (*red*). The concentrations are smaller for stretch transverse to the beam, but they are still there. Only a tiny region in the broken beam seems to have lower stretch. Hence, for either stretch direction, partial loss of a beam induces much larger deformations in the neural tissues than complete loss of a beam.

remodeling[5,60,66] and glaucoma likely take place at the pore/beam scale, or even lower, we believe that the results in this work are important.

We are not aware of other quantitative studies on the biomechanical role of LC defects. To model LC defects, we leveraged our development of polarized light microscopy methods for measuring collagen birefringence and alignment at the submicron scale.[28–36] We considered LC defects of multiple sizes with the approach of progressively removing beams so that the models can be directly compared. When we removed a beam, we replaced it with neural tissues. This is because optical coherence tomography scans[50,51] and histology images[20] suggest that LC defects are filled by neural tissues. Readers should be careful and not interpret our results in terms of tissue remodeling or defect progression, as simulating remodeling or defect progression might have required replacing a removed or "broken" beam by some scar-like material that is stiffer than neural tissues. As long as the material replacing the LC beam is more compliant than the original beam, the effects we predict should be present, albeit to a different extent.

We modeled LC defects at the periphery of the lamina for two reasons. First, optical coherence tomography scans show that LC defects are often located at the periphery of the lamina.[14,18,40] Second, evidence from ex vivo[56,67–70] and in vivo[44,71–74] studies suggest that neural tissues at the periphery of the lamina often experience the largest IOP-induced strains. Modeling defects in this region can provide an upper-bound estimation of the influence of LC defects on IOP-induced mechanical insult to neural tissues.

The rationale, consequences, and limitations of the choices of model geometry and mechanical properties, and of the multiscale modeling approach used have been

Investigative Ophthalmology & Visual Science

discussed previously[21,22] and so are not discussed at length again here. Instead, below is a summary of earlier discussions, with a focus on limitations and considerations most relevant to this work.

First, models developed in this work were based on sheep rather than human eyes. Sheep and human eyes share several fundamental characteristics, including the trabecular structure of lamina and overall connective tissue architecture of sclera.[31] Therefore, it seems plausible that our findings based on sheep eyes will extend to human eyes. Nevertheless, this must still be validated. Although sheep can develop glaucoma,[75] to the best of our knowledge, it remains unknown if sheep LCs also have defects.

Second, our models were 3D with thickness, but flat in the sense of not having curvature. Although the usefulness of this modeling approach for optic nerve head biomechanics has been demonstrated,[21,22,24] our models do not incorporate the curvature and out-of-plane orientation of the lamina beams and retinal ganglion cell axons, which could be important. Our models allow the study of LC responses to in-plane stresses, which are thought to be larger, and more influential, than the out-of-plane stresses.[24] Hence, we believe that these models are meaningful and useful as a first approximation. Although the models incorporate realistic beam cross sections, further work is needed to incorporate the complex 3D structure of the beams and pores, which likely affect local insult.[29,35,37,60]

Third, our models did not include the bending or bulging of the LC. Including bending is an important next step that also adds substantial complexity but could be crucial to the tissue response. More experimental information is necessary to develop and validate 3D models of LC mechanics, such as full 3D fiber information[36] and detailed deformation measures during inflation.[76,77]

Fourth, to mimic the effects of IOP elevation, we applied an outward boundary pressure of 10 times of IOP to the edge of the mesoscale model. This assumption is justified based on one of the fundamental principles of mechanics, the law of Laplace, which states that the in-plane stress (i.e., hoop stress) in a thin spherical shell will be many times greater than the pressure inside the shell. This assumption has been employed frequently in biomechanics[78–80] and, in particular, ocular biomechanics.[21,22,24,81–83] Note that the use of Laplace's law also assumes that the distribution of hoop stress is constant across the edge of the mesoscale model, ignoring subtle variations due to changes in regional thickness. We reasoned that this assumption would have only minor influences on our results.

Fifth, the displacement boundary conditions applied to all of the microscale models were the same. Collagen density in the lamina decreases with the size of the defect and thus the structural stiffness of the lamina. This may result in an increased displacement at the boundary because a structurally weaker lamina would be stretched more under loads of IOP. However, even for the largest defect that we considered (i.e., 12 beams removed), the decrease in the collagen density of the entire lamina is very small. This allowed us to simplify the procedure for assigning displacement boundary conditions.

Sixth, in our mesoscale model, we assigned the hyperelastic properties of the LC based on those of the sclera,[38] with the strain energy density weighted by the density of collagen fibers. We made this approximation because experimentally measured LC properties are not available. Given that type I collagen is a principal load-bearing component of both the LC and sclera,[84] we deemed this to be a reasonable approximation.

Seventh, our models considered neural tissues and collagen beams in the LC as homogeneous continuums. In reality, neural tissues are composed of mixtures of retinal ganglion cell axons and glial cells that bind to each other and to collagen beams through transmembrane biomechanical bonds such as cadherins and integrins.[52] These bonds may fail under high strains and thus alter the deformation of axons and neural tissues. Likewise, we assumed that collagen beams are composed of a family of collagen fibers that undergo affine deformations. In fact, studies have shown in other tissues that collagen fibrils and fibers may undergo non-affine deformations at the microscale, particularly when loaded in the cross-fiber direction.[85,86] Given the length scale of the LC beams (i.e., ~15–100 μm) and the fact that collagen in beams is aligned along the direction of loading, we suspect that our assumption of affine deformations is reasonable. Nonetheless, experimental studies using higher resolution imaging techniques, such as polarization-sensitive second-harmonic generation microscopy,[87–89] would be needed to verify this assumption.

Eighth, we did not consider the effects of interactions between LC defects and collagen beam mechanical properties. In a recent study,[35] we showed that collagen microstructure of LC beams varies among beams, suggesting that their mechanical properties also vary. In this sense, it is possible that the LCs with defects have mechanical properties distinct from those without defects, even at the local beam or neural tissue level.

Finally, although we made multiple models, all the results shown herein are of a single location of a single eye. Other locations or eyes will likely have different responses, and we remind the readers that the specific values we report are unlikely to apply elsewhere exactly. However, we have also shown that the mechanism underlying the findings is fairly general, suggesting that the fundamental results likely extend to other locations or eyes, as long as the assumptions of the model hold. We note here, however, that our assumptions are not much different from those of many other numerical models of the LC. Modeling more regions or eyes would be necessary understand the differences between them and to predict the causes and consequences of defects in a specific eye.

In conclusion, our microstructure-based models predict that missing LC beams may mitigate IOP-induced neural tissue insult, suggesting that the role of LC connective tissues is more complex than simply fortifying against IOP. Our models further predict that partial loss of a beam is biomechanically much worse than complete loss of a beam, perhaps explaining why defects have been reported clinically but partial beams have not. The mechanisms underlying our findings appear relatively general. We should point out that given the complexity of the LC architecture and biomechanics, our work does not completely rule out the possibility that some LC defects could increase neural tissue insult. Our intent in this work was to show that, contrary to prevailing thought, some so-called LC defects can lead to decreased IOP-induced neural tissues. The knowledge of how LC defects alter IOP-induced mechanical insult to neural tissues will enhance our interpretation of clinical observations of LC defects in glaucomatous eyes.

Investigative Ophthalmology & Visual Science

Acknowledgments

Supported in part by grants from the National Institutes of Health (R01-EY023966, R01-EY025011, R01-EY028662, P30-EY008098, and T32-EY017271), the Eye and Ear Foundation of Pittsburgh, and Research to Prevent Blindness. The work was conducted while APV and BLB were at the University of Pittsburgh; APV now works for Johnson & Johnson, and BLB now works at Baxter International.

Disclosure: **A.P. Voorhees**, None; **Y. Hua**, None; **B.L. Brazile**, None; **B. Wang**, None; **S. Waxman**, None; **J.S. Schuman**, intellectual property licensed by MIT to Carl Zeiss Meditec (F); **I.A. Sigal**, None

References

1. Park SC, Hsu AT, Su D, et al. Factors associated with focal lamina cribrosa defects in glaucoma. *Invest Ophthalmol Vis Sci*. 2013;54(13):8401–8407.
2. Park HY, Hwang YS, Park CK. Ocular characteristics associated with the location of focal lamina cribrosa defects in open-angle glaucoma patients. *Eye (Lond)*. 2017;31(4):578–587.
3. Mistry V, An D, Barry CJ, House PH, Morgan WH. Association between focal lamina cribrosa defects and optic disc haemorrhage in glaucoma. *Br J Ophthalmol*. 2020;104(1):98–103.
4. Downs JC, Girkin CA. Lamina cribrosa in glaucoma. *Curr Opin Ophthalmol*. 2017;28(2):113–119.
5. Grytz R, Girkin CA, Libertiaux V, Downs JC. Perspectives on biomechanical growth and remodeling mechanisms in glaucoma. *Mech Res Commun*. 2012;42:92–106.
6. Sigal IA, Ethier CR. Biomechanics of the optic nerve head. *Exp Eye Res*. 2009;88(4):799–807.
7. Roberts MD, Sigal IA, Liang Y, Burgoyne CF, Downs JC. Changes in the biomechanical response of the optic nerve head in early experimental glaucoma. *Invest Ophthalmol Vis Sci*. 2010;51(11):5675–5684.
8. Sigal IA, Flanagan JG, Tertinegg I, Ethier CR. Finite element modeling of optic nerve head biomechanics. *Invest Ophthalmol Vis Sci*. 2004;45(12):4378–4387.
9. Behkam R, Kollech HG, Jana A, et al. Racioethnic differences in the biomechanical response of the lamina cribrosa. *Acta Biomater*. 2019;88:131–140.
10. Ling YTT, Shi R, Midgett DE, Jefferys JL, Quigley HA, Nguyen TD. Characterizing the collagen network structure and pressure-induced strains of the human lamina cribrosa. *Invest Ophthalmol Vis Sci*. 2019;60(7):2406–2422.
11. Albon J, Farrant S, Akhtar S, et al. Connective tissue structure of the tree shrew optic nerve and associated ageing changes. *Invest Ophthalmol Vis Sci*. 2007;48(5):2134–2144.
12. Burgoyne CF, Downs JC, Bellezza AJ, Suh JK, Hart RT. The optic nerve head as a biomechanical structure: a new paradigm for understanding the role of IOP-related stress and strain in the pathophysiology of glaucomatous optic nerve head damage. *Prog Retin Eye Res*. 2005;24(1):39–73.
13. Tan NY, Koh V, Girard MJ, Cheng CY. Imaging of the lamina cribrosa and its role in glaucoma: a review. *Clin Exp Ophthalmol*. 2018;46(2):177–188.
14. Lee EJ, Han JC, Kee C. A novel hypothesis for the pathogenesis of glaucomatous disc hemorrhage. *Prog Retin Eye Res*. 2017;60:20–43.
15. Sigal IA, Wang B, Strouthidis NG, Akagi T, Girard MJ. Recent advances in OCT imaging of the lamina cribrosa. *Br J Ophthalmol*. 2014;98(suppl 2):ii34–ii39.
16. Faridi OS, Park SC, Kabadi R, et al. Effect of focal lamina cribrosa defect on glaucomatous visual field progression. *Ophthalmology*. 2014;121(8):1524–1530.
17. Kwun Y, Han G, Choy Y-J, Han JC, Kee C. Optic disc characteristics and visual field progression in normal tension glaucoma patients with tilted optic discs. *J Glaucoma*. 2016;25(11):901–907.
18. Kiumehr S, Park SC, Dorairaj S, et al. In vivo evaluation of focal lamina cribrosa defects in glaucoma. *Arch Ophthalmol*. 2012;130(5):552–559.
19. Sawada Y, Araie M, Kasuga H, et al. Focal lamina cribrosa defect in myopic eyes with nonprogressive glaucomatous visual field defect. *Am J Ophthalmol*. 2018;190:34–49.
20. Girkin CA, Wang L, Downs JCC, Yang H, Kankipati L, Burgoyne CF. Laminar disinsertion from the neural canal observed in three-dimensional reconstruction of human glaucomatous optic nerves. *Invest Ophthalmol Vis Sci*. 2011;52:3957–3957.
21. Voorhees AP, Jan NJ, Austin ME, et al. Lamina cribrosa pore shape and size as predictors of neural tissue mechanical insult. *Invest Ophthalmol Vis Sci*. 2017;58(12):5336–5346.
22. Voorhees AP, Jan NJ, Sigal IA. Effects of collagen microstructure and material properties on the deformation of the neural tissues of the lamina cribrosa. *Acta Biomater*. 2017;58:278–290.
23. Sigal IA, Flanagan JG, Ethier CR. Factors influencing optic nerve head biomechanics. *Invest Ophthalmol Vis Sci*. 2005;46(11):4189–4199.
24. Zhang L, Albon J, Jones H, et al. Collagen microstructural factors influencing optic nerve head biomechanics. *Invest Ophthalmol Vis Sci*. 2015;56(3):2031–2042.
25. Voorhees A, Grimm J, Bilonick R, et al. What is a typical optic nerve head? *Exp Eye Res*. 2016;149:40–47.
26. Voorhees AP, Jan N-J, Hua Y, Yang B, Sigal IA. Peripapillary sclera architecture revisited: a tangential fiber model and its biomechanical implications. *Acta Biomater*. 2018;79:113–122.
27. Hua Y, Voorhees AP, Sigal IA. Cerebrospinal fluid pressure: revisiting factors influencing optic nerve head biomechanics. *Invest Ophthalmol Vis Sci*. 2018;59(1):154–165.
28. Jan NJ, Grimm JL, Tran H, et al. Polarization microscopy for characterizing fiber orientation of ocular tissues. *Biomed Opt Express*. 2015;6(12):4705–4718.
29. Jan NJ, Lathrop K, Sigal IA. Collagen architecture of the posterior pole: high-resolution wide field of view visualization and analysis using polarized light microscopy. *Invest Ophthalmol Vis Sci*. 2017;58(2):735–744.
30. Gogola A, Jan N-J, Brazile B, et al. Spatial patterns and age-related changes of the collagen crimp in the human cornea and sclera. *Invest Ophthalmol Vis Sci*. 2018;59(7):2987–2998.
31. Gogola A, Jan N-J, Lathrop KL, Sigal IA. Radial and circumferential collagen fibers are a feature of the peripapillary sclera of human, monkey, pig, cow, goat, and sheep. *Invest Ophthalmol Vis Sci*. 2018;59(12):4763–4774.
32. Jan N-J, Gomez C, Moed S, et al. Microstructural crimp of the lamina cribrosa and peripapillary sclera collagen fibers. *Invest Ophthalmol Vis Sci*. 2017;58(9):3378–3388.
33. Jan N-J, Sigal IA. Collagen fiber recruitment: a microstructural basis for the nonlinear response of the posterior pole of the eye to increases in intraocular pressure. *Acta Biomater*. 2018;72:295–305.
34. Jan N-J, Brazile BL, Hu D, et al. Crimp around the globe; patterns of collagen crimp across the corneoscleral shell. *Exp Eye Res*. 2018;172:159–170.

Investigative Ophthalmology & Visual Science

35. Brazile BL, Hua Y, Jan N-J, Wallace J, Gogola A, Sigal IA. Thin lamina cribrosa beams have different collagen microstructure than thick beams. *Invest Ophthalmol Vis Sci*. 2018;59(11):4653–4661.
36. Yang B, Jan NJ, Brazile B, Voorhees A, Lathrop KL, Sigal IA. Polarized light microscopy for 3-dimensional mapping of collagen fiber architecture in ocular tissues. *J Biophotonics*. 2018;11(8):e201700356.
37. Campbell IC, Coudrillier B, Mensah J, Abel RL, Ethier CR. Automated segmentation of the lamina cribrosa using Frangi's filter: a novel approach for rapid identification of tissue volume fraction and beam orientation in a trabeculated structure in the eye. *J R Soc Interface*. 2015;12(104):20141009.
38. Coudrillier B, Boote C, Quigley HA, Nguyen TD. Scleral anisotropy and its effects on the mechanical response of the optic nerve head. *Biomech Model Mechanobiol*. 2013;12(5):941–963.
39. Chung CW, Girard MJ, Jan N-J, Sigal IA. Use and misuse of Laplace's law in ophthalmology. *Invest Ophthalmol Vis Sci*. 2016;57(1):236–245.
40. Lee EJ, Kim T-W, Kim M, Girard MJ, Mari JM, Weinreb RN. Recent structural alteration of the peripheral lamina cribrosa near the location of disc hemorrhage in glaucoma. *Invest Ophthalmol Vis Sci*. 2014;55(4):2805–2815.
41. Galle B, Ouyang H, Shi R, Nauman E. A transversely isotropic constitutive model of excised guinea pig spinal cord white matter. *J Biomech*. 2010;43(14):2839–2843.
42. Weickenmeier J, de Rooij R, Budday S, Ovaert TC, Kuhl E. The mechanical importance of myelination in the central nervous system. *J Mech Behav Biomed Mater*. 2017;76:119–124.
43. Sigal IA, Flanagan JG, Tertinegg I, Ethier CR. Predicted extension, compression and shearing of optic nerve head tissues. *Exp Eye Res*. 2007;85(3):312–322.
44. Fazio MA, Clark ME, Bruno L, Girkin CA. In vivo optic nerve head mechanical response to intraocular and cerebrospinal fluid pressure: imaging protocol and quantification method. *Sci Rep*. 2018;8(1):12639.
45. Maas SA, Ellis BJ, Ateshian GA, Weiss JA. FEBio: finite elements for biomechanics. *J Biomech Eng*. 2012;134(1):011005.
46. Moerman KM. GIBBON: the geometry and image-based bioengineering add-on. *J Open Source Softw*. 2018;3(22):506.
47. Flynn BP, Bhole AP, Saeidi N, Liles M, DiMarzio CA, Ruberti JW. Mechanical strain stabilizes reconstituted collagen fibrils against enzymatic degradation by mammalian collagenase matrix metalloproteinase 8 (MMP-8). *PLoS One*. 2010;5(8):e12337.
48. Bhole AP, Flynn BP, Liles M, Saeidi N, Dimarzio CA, Ruberti JW. Mechanical strain enhances survivability of collagen micronetworks in the presence of collagenase: implications for load-bearing matrix growth and stability. *Philos Trans A Math Phys Eng Sci*. 2009;367(1902):3339–3362.
49. Ruberti JW, Hallab NJ. Strain-controlled enzymatic cleavage of collagen in loaded matrix. *Biochem Biophys Res Commun*. 2005;336(2):483–489.
50. Takayama K, Hangai M, Kimura Y, et al. Three-dimensional imaging of lamina cribrosa defects in glaucoma using swept-source optical coherence tomography. *Invest Ophthalmol Vis Sci*. 2013;54(7):4798–4807.
51. Kimura Y, Akagi T, Hangai M, et al. Lamina cribrosa defects and optic disc morphology in primary open angle glaucoma with high myopia. *PLoS One*. 2014;9(12):e115313.
52. Elkington A, Inman C, Steart P, Weller R. The structure of the lamina cribrosa of the human eye: an immunocytochemical and electron microscopical study. *Eye (Lond)*. 1990;4(pt 1):42–57.
53. Roberts MD, Liang Y, Sigal IA, et al. Correlation between local stress and strain and lamina cribrosa connective tissue volume fraction in normal monkey eyes. *Invest Ophthalmol Vis Sci*. 2010;51(1):295–307.
54. Barou O, Valentin D, Vico L, et al. High-resolution three-dimensional micro-computed tomography detects bone loss and changes in trabecular architecture early: comparison with DEXA and bone histomorphometry in a rat model of disuse osteoporosis. *Invest Radiol*. 2002;37(1):40–46.
55. Lang T, LeBlanc A, Evans H, Lu Y, Genant H, Yu A. Cortical and trabecular bone mineral loss from the spine and hip in long-duration spaceflight. *J Bone Miner Res*. 2004;19(6):1006–1012.
56. Sigal IA, Grimm JL, Jan NJ, Reid K, Minckler DS, Brown DJ. Eye-specific IOP-induced displacements and deformations of human lamina cribrosa. *Invest Ophthalmol Vis Sci*. 2014;55(1):1–15.
57. Sigal IA. Interactions between geometry and mechanical properties on the optic nerve head. *Invest Ophthalmol Vis Sci*. 2009;50(6):2785–2795.
58. Sigal IA, Flanagan JG, Tertinegg I, Ethier CR. Modeling individual-specific human optic nerve head biomechanics. Part I: IOP-induced deformations and influence of geometry. *Biomech Model Mechanobiol*. 2009;8(2):85–98.
59. Sigal IA, Flanagan JG, Tertinegg I, Ethier CR. Modeling individual-specific human optic nerve head biomechanics. Part II: influence of material properties. *Biomech Model Mechanobiol*. 2009;8(2):99–109.
60. Roberts MD, Grau V, Grimm J, et al. Remodeling of the connective tissue microarchitecture of the lamina cribrosa in early experimental glaucoma. *Invest Ophthalmol Vis Sci*. 2009;50(2):681–690.
61. Yang H, Downs JC, Sigal IA, Roberts MD, Thompson H, Burgoyne CF. Deformation of the normal monkey optic nerve head connective tissue after acute IOP elevation within 3-D histomorphometric reconstructions. *Invest Ophthalmol Vis Sci*. 2009;50(12):5785–5799.
62. Feola AJ, Myers JG, Raykin J, et al. Finite element modeling of factors influencing optic nerve head deformation due to intracranial pressure. *Invest Ophthalmol Vis Sci*. 2016;57(4):1901–1911.
63. Yang H, Reynaud J, Lockwood H, et al. The connective tissue phenotype of glaucomatous cupping in the monkey eye - clinical and research implications. *Prog Retin Eye Res*. 2017;59:1–52.
64. Liou J-J, Drewry MD, Sweeney A, Brown BN, Geest JPV. Decellularizing the porcine optic nerve head: toward a model to study the mechanobiology of glaucoma. *Transl Vis Sci Technol*. 2020;9(8):17.
65. Hopkins AA, Murphy R, Irnaten M, Wallace DM, Quill B, O'Brien C. The role of lamina cribrosa tissue stiffness and fibrosis as fundamental biomechanical drivers of pathological glaucomatous cupping. *Am J Physiol Cell Physiol*. 2020;319(4):C611–C623.
66. Grytz R, Sigal IA, Ruberti JW, Meschke G, Downs JC. Lamina cribrosa thickening in early glaucoma predicted by a microstructure motivated growth and remodeling approach. *Mech Mater*. 2012;44:99–109.
67. Midgett DE, Pease ME, Jefferys JL, et al. The pressure-induced deformation response of the human lamina cribrosa: analysis of regional variations. *Acta Biomater*. 2017;53:123–139.
68. Midgett DE, Jefferys JL, Quigley HA, Nguyen TD. The contribution of sulfated glycosaminoglycans to the inflation response of the human optic nerve head. *Invest Ophthalmol Vis Sci*. 2018;59(7):3144–3154.
69. Coudrillier B, Geraldes DM, Vo NT, et al. Phase-contrast micro-computed tomography measurements of the intraoc-

Investigative Ophthalmology & Visual Science

ular pressure-induced deformation of the porcine lamina cribrosa. *IEEE Trans Med Imaging*. 2016;35(4):988–999.

70. Coudrillier B, Campbell IC, Read AT, et al. Effects of peripapillary scleral stiffening on the deformation of the lamina cribrosa. *Invest Ophthalmol Vis Sci*. 2016;57(6):2666–2677.
71. Tran H, Grimm J, Wang B, et al. Mapping in-vivo optic nerve head strains caused by intraocular and intracranial pressures. *Proc SPIE Int Soc Opt Eng*. 2017;10067:100670B.
72. Tran H, Wallace J, Zhu Z, et al. Seeing the hidden lamina: effects of exsanguination on the optic nerve head. *Invest Ophthalmol Vis Sci*. 2018;59(6):2564–2575.
73. Girard MJ, Beotra MR, Chin KS, et al. In vivo 3-dimensional strain mapping of the optic nerve head following intraocular pressure lowering by trabeculectomy. *Ophthalmology*. 2016;123(6):1190–1200.
74. Beotra MR, Wang X, Tun TA, et al. In vivo three-dimensional lamina cribrosa strains in healthy, ocular hypertensive, and glaucoma eyes following acute intraocular pressure elevation. *Invest Ophthalmol Vis Sci*. 2018;59(1):260–272.
75. Gerometta R, Podos SM, Danias J, Candia OA. Steroid-induced ocular hypertension in normal sheep. *Invest Ophthalmol Vis Sci*. 2009;50(2):669–673.
76. Wei J, Yang B, Voorhees AP, et al. Measuring in-vivo and in-situ ex-vivo the 3D deformation of the lamina cribrosa microstructure under elevated intraocular pressure. *Proc SPIE*. 2018;10496:1–7.
77. Brazile BL, Yang B, Waxman S, et al. Lamina cribrosa capillaries straighten as intraocular pressure increases. *Invest Ophthalmol Vis Sci*. 2020;61(12):2.
78. Voorhees AP, Han H-C. A model to determine the effect of collagen fiber alignment on heart function post myocardial infarction. *Theor Biol Med Model*. 2014;11:6.
79. Jackson FW, Adrain AL, Black M, Miller LS. Calculation of esophageal variceal wall tension by direct sonographic and manometric measurements. *Gastrointest Endosc*. 1999;50(2):247–251.
80. Zhong L, Ghista D, Tan R. Left ventricular wall stress compendium. *Comput Methods Biomech Biomed Engin*. 2012;15(10):1015–1041.
81. Sander E, Downs J, Hart R, Burgoyne C, Nauman E. A cellular solid model of the lamina cribrosa: mechanical dependence on morphology. *J Biomech Eng*. 2006;128(6):879–889.
82. Palko JR, Morris HJ, Pan X, et al. Influence of age on ocular biomechanical properties in a canine glaucoma model with ADAMTS10 mutation. *PLoS One*. 2016;11(6):e0156466.
83. Cahane M, Bartov E. Axial length and scleral thickness effect on susceptibility to glaucomatous damage: a theoretical model implementing Laplace's law. *Ophthalmic Res*. 1992;24(5):280–284.
84. Albon J, Karwatowski W, Avery N, Easty DL, Duance VC. Changes in the collagenous matrix of the aging human lamina cribrosa. *Br J Ophthalmol*. 1995;79(4):368–375.
85. Lake SP, Cortes DH, Kadlowec JA, Soslowsky LJ, Elliott DM. Evaluation of affine fiber kinematics in human supraspinatus tendon using quantitative projection plot analysis. *Biomech Model Mechanobiol*. 2012;11(1–2):197–205.
86. Hepworth D, Steven-Fountain A, Bruce D, Vincent J. Affine versus non-affine deformation in soft biological tissues, measured by the reorientation and stretching of collagen fibres through the thickness of compressed porcine skin. *J Biomech*. 2001;34(3):341–346.
87. Vohnsen B, Li J, Jan N-J, Sigal IA. Vectorial 3-D polarization second-harmonic imaging of collagen fibril organization in the lamina cribrosa. *Paper presented at 18th European Light Microscopy Initiative Meeting, June 5–8, 2018, Dublin, Ireland*. 2018.
88. Lee P-Y, Yang B, Sigal IA. Real-time measurement of collagen architecture and deformations at sub-micron resolution. *Summer Biomechanics, Bioengineering, and Biotransport Conference, June 25–28, 2019, Seven Springs, PA*. 2019.
89. Lee P-Y, Yang B, Zhu Z, Ji F, Hua Y, Sigal IA. Microstructural evidence that lamina cribrosa beams (LC), peripapillary sclera (PPS) and central retinal artery (CRA) have distinct mechanical behaviors when stretched. *Invest Ophthalmol Vis Sci*. 2020;61(7):4783–4783.

Investigative Ophthalmology & Visual Science